

Differentiable Voronoi Diagrams for Simulation of Cell-Based Mechanical Systems

LOGAN NUMEROW, ETH Zürich, Switzerland

YUE LI, ETH Zürich, Switzerland

STELIAN COROS, ETH Zürich, Switzerland

BERNHARD THOMASZEWSKI, ETH Zürich, Switzerland

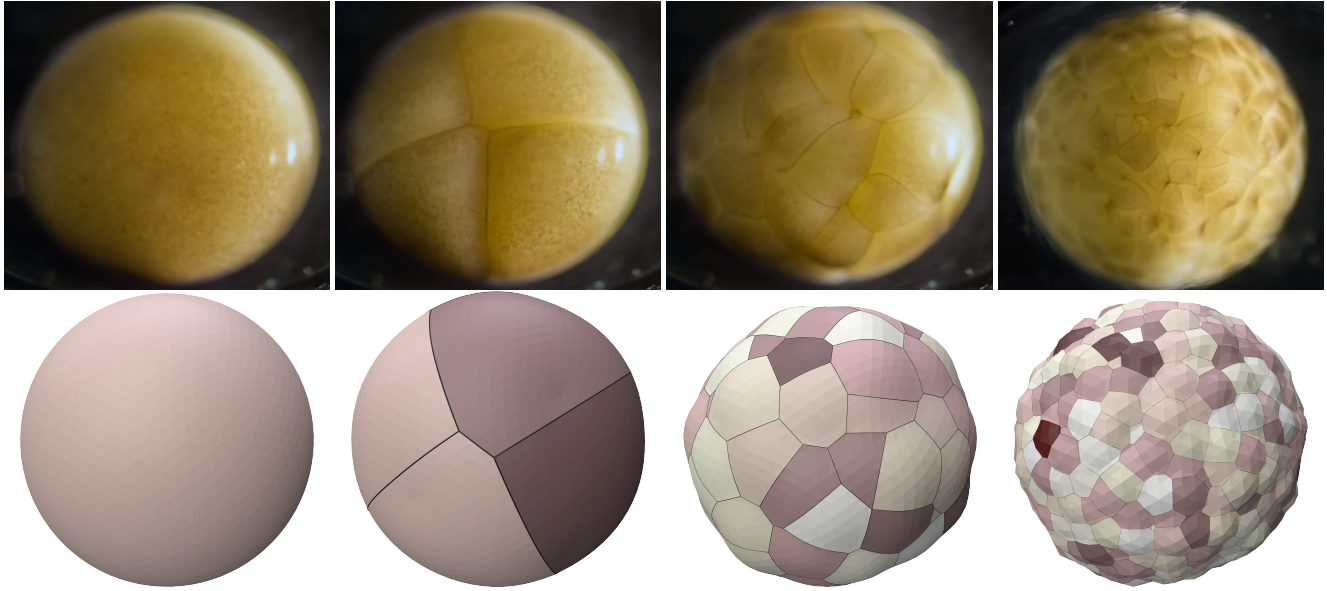


Fig. 1. We use differentiable Voronoi diagrams to simulate embryonic cleavage in an elastic spherical membrane. *Bottom*: As cells split according to a predefined schedule, substantial neighborhood changes and cell deformations occur. Each cell is modeled using only a single Voronoi site carrying four degrees of freedom. *Top*: Images from Jan van Ijken’s “Becoming” [2018], depicting the embryonic development of a salamander, are included for comparison.

Navigating topological transitions in cellular mechanical systems is a significant challenge for existing simulation methods. While abstract models lack predictive capabilities at the cellular level, explicit network representations struggle with topology changes, and per-cell representations are computationally too demanding for large-scale simulations. To address these challenges, we propose a novel cell-centered approach based on differentiable Voronoi diagrams. Representing each cell with a Voronoi site, our method defines shape and topology of the interface network implicitly. In this way, we substantially reduce the number of problem variables, eliminate the need for explicit contact handling, and ensure continuous geometry changes during topological transitions. Closed-form derivatives of network

Authors’ addresses: Logan Numerow, ETH Zürich, Switzerland, lnumerow@student.ethz.ch; Yue Li, ETH Zürich, Switzerland, yue.li@inf.ethz.ch; Stelian Coros, ETH Zürich, Switzerland, stelian.coros@inf.ethz.ch; Bernhard Thomaszewski, ETH Zürich, Switzerland, bthomasz@ethz.ch.

Permission to make digital or hard copies of all or part of this work for personal or classroom use is granted without fee provided that copies are not made or distributed for profit or commercial advantage and that copies bear this notice and the full citation on the first page. Copyrights for components of this work owned by others than the author(s) must be honored. Abstracting with credit is permitted. To copy otherwise, or republish, to post on servers or to redistribute to lists, requires prior specific permission and/or a fee. Request permissions from permissions@acm.org.

© 2024 Copyright held by the owner/author(s). Publication rights licensed to ACM. 0730-0301/2024/7-ART69 \$15.00 <https://doi.org/10.1145/3658152>

positions facilitate simulation with Newton-type methods for a wide range of per-cell energies. Finally, we extend our differentiable Voronoi diagrams to enable coupling with arbitrary rigid and deformable boundaries. We apply our approach to a diverse set of examples, highlighting splitting and merging of cells as well as neighborhood changes. We illustrate applications to inverse problems by matching soap foam simulations to real-world images. Comparative analysis with explicit cell models reveals that our method achieves qualitatively comparable results at significantly faster computation times.

CCS Concepts: • **Computing methodologies** → **Physical simulation**.

Additional Key Words and Phrases: Voronoi Diagram, Power Diagram, Foam Simulation, Differentiable Simulation

ACM Reference Format:

Logan Numerow, Yue Li, Stelian Coros, and Bernhard Thomaszewski. 2024. Differentiable Voronoi Diagrams for Simulation of Cell-Based Mechanical Systems. *ACM Trans. Graph.* 43, 4, Article 69 (July 2024), 11 pages. <https://doi.org/10.1145/3658152>

1 INTRODUCTION

A central characteristic of cellular mechanical systems is that cells change neighborhoods during dynamic motion and growth-induced splitting (as in biological tissue), or through merging and collapse

(as in soap foams). These topological transitions cause abrupt force changes, which make computational modeling very challenging.

There are several existing approaches in the literature for simulation of cell-based systems. One option is to abstract away the cellular structure and model the large-scale mechanics of the system in a homogenized sense. Evidently, such models cannot predict interactions at the cellular level governed by local topology changes. Another approach is to explicitly model the network of cell interfaces, enabling efficient computation of cell volumes and other geometric quantities that influence their mechanics. However, topology changes are difficult to model with explicit network representations, requiring discrete mesh adaptations and other discontinuous operations. Another class of models represents each cell individually using, *e.g.*, per-cell finite element discretizations. While this approach allows for accurate modeling of cell interactions, it requires a very large number of degrees of freedom to resolve cell deformations, and contact must be handled explicitly at every cell interface. These aspects render this strategy unsuitable for large-scale simulations involving hundreds or thousands of cells.

To overcome the limitations of existing methods, we propose a novel cell-centered approach based on generalized Voronoi diagrams. Each cell is represented by a Voronoi *site*, and the topology and shape of the cells are defined implicitly. This representation uses far fewer degrees of freedom, avoids explicit handling of contact between cells, and ensures continuous cell geometry changes through topological transitions. In order to use this Voronoi model for simulation, we derive closed-form expressions for first and second derivatives of cell geometry with respect to site positions, allowing us to use Newton-type optimization solvers for a wide range of energies. We furthermore obtain equilibrium-state derivatives of the interface network using sensitivity analysis, thus opening the door to a wide range of inverse simulation problems. Finally, we extend our differentiable Voronoi formulation to enable coupling with arbitrary rigid and deformable boundaries.

We demonstrate the potential of our method on a diverse set of examples, including tissue growth and foam coarsening. We furthermore show applications of differentiable Voronoi diagrams to inverse problems by optimizing per-cell pressures to match input images from real-world foams. Our comparison with explicit cell models indicates that differentiable Voronoi diagrams can produce qualitatively similar behavior with much faster computation times.

2 RELATED WORK

Simulating Cell & Tissue Dynamics. Various computational models have been developed to simulate cell-based mechanical systems. One approach is to abstract away the cellular structure and model the mechanical properties of the system in an averaged sense at coarser scales [Brodland et al. 2006; Kondo et al. 2018; Piatnitski and Ptashnyk 2020]. Our focus, however, is on problems that are governed by cell-level phenomena. One option in this context is to explicitly model the network of cell interfaces using so-called *vertex models* [Alt et al. 2017; Fletcher et al. 2014; Honda et al. 2004]. Although extensions have been developed to allow for topology changes [Farhadifar et al. 2007; Okuda et al. 2012], the discrete mesh modifications involved in these methods are problematic for

differentiable simulation. Moreover, explicit vertex models require additional constraints to prevent self-intersections and other invalid geometry [Vedel-Larsen 2010]. Our differentiable Voronoi diagrams, in contrast, ensure a valid interface network at all times and guarantee continuous topology changes for any displacement of the Voronoi sites.

Another line of work has explored so-called *deformable cell models*, in which cells are represented through separate surface meshes [Conradin et al. 2021; Kim et al. 2021]. While this approach enables accurate modeling of contact forces and topology changes, it requires explicit handling of collisions between cells. Moreover, hundreds to thousands of degrees of freedom are needed per cell, which rapidly leads to all but intractable problem size. With each cell encoded by the position of a single Voronoi site, our approach requires dramatically fewer degrees of freedom. The resulting model is highly scalable, enabling efficient gradient-based optimization with thousands of cells.

Simulating Soap Films, Foams, & Bubbles. The dynamics of bubbles have attracted substantial interest from the graphics community. Examples include the formation of bubbles in water [Hong et al. 2008], soap film dynamics [Deng et al. 2022; Huang et al. 2020; Ishida et al. 2020], and general foams [Busaryev et al. 2012]. Various representations have been explored, ranging from explicit surface meshes [Da et al. 2015] to mixed particle-and-grid discretizations [Goldade et al. 2020]. We show that, using only a single site per foam cell, differentiable Voronoi diagrams can produce realistic 3D foam coarsening simulations. Our method can likewise be used for inverse problems such as matching soap film simulations to real-world images.

Implicit Voronoi Diagrams. Voronoi diagrams have numerous applications in computer graphics, vision, and beyond. They have been explored as a basis for, *e.g.*, fluid [de Goes et al. 2015] and foam [Busaryev et al. 2012] simulations, image segmentation [Williams et al. 2020] as well as for structural design. Zhang *et al.* [2017] design personalized medical braces represented as centroidal Voronoi diagrams. Their algorithm uses a variant of Lloyd’s method to iteratively adjust site positions in order to minimize the design objective. Lumpe *et al.* [2022] investigate power diagrams for topology optimization. While cell volumes are adapted in each iteration, all simulations are performed on finite element meshes generated from the power diagrams. Also targeting topology optimization, Feng *et al.* [2022] introduce a smooth relaxation of Voronoi diagrams based on *softmax* functions. However, their approach ultimately requires rasterization on a Cartesian grid for optimization.

We refer to the aforementioned Voronoi models as *implicit Voronoi diagrams*, as the simulated structures are defined implicitly by Voronoi sites rather than with explicit degrees of freedom. Lloyd’s algorithm [1982] for generating centroidal Voronoi tessellations (CVT) is arguably the most widely used method for optimization of Voronoi diagrams. Nevertheless, substantial accelerations can be achieved when using gradient-based or quasi-Newton methods [Liu et al. 2009; Wang et al. 2015; Yan et al. 2009, 2011]. Unlike these methods, our work provides explicit derivatives of Voronoi vertices, opening the door to general energy functions that can be adapted to a large variety of physical systems. In addition, we provide an

algebraic recipe for unified treatment of Voronoi cell faces and clipping geometry, enabling simulation of cellular systems coupled to moving or deformable boundaries.

Adaptive Meshes. Adapting meshes to ensure given quality criteria is a common strategy in many simulation contexts, including large elastoplastic deformations [Bargteil et al. 2007; Wicke et al. 2010; Wojtan et al. 2009], fracture [Koschier et al. 2014; O’Brien et al. 2002; Pfaff et al. 2014], fluid flow [Misztal et al. 2014], and the folding of thin sheet materials [Narain et al. 2013, 2012; Schreck et al. 2016; Zhang et al. 2022]. Remeshing is typically applied as a post-process after each time step, which can disturb force equilibrium and lead to abrupt configuration changes. Coupling remeshing with time integration can avoid such artifacts [Ferguson et al. 2023]. While mesh adaptation is often an optional improvement, topological changes that occur, e.g., during droplet formation make remeshing compulsory [Brochu and Bridson 2009]. The applications that we consider in this work likewise involve inherent topology changes as cells split, collapse, or switch neighbors. However, our differentiable Voronoi diagrams eliminate the need for explicit remeshing, as the mesh is given implicitly through the Voronoi sites.

Equilibrium-Constrained Optimization. Differentiable simulation is a core technology for solving equilibrium-constrained optimization problems in graphics and beyond. Examples include material parameter estimation [Bickel et al. 2009; Hahn et al. 2019; Miguel et al. 2012; Yan et al. 2018], elastic shape optimization [Chen et al. 2014; Ly et al. 2018; Panetta et al. 2017], inflatables [Panetta et al. 2021; Skouras et al. 2014], clothing design [Montes et al. 2020; Umetani et al. 2011; Wang 2018], and trajectory optimization [Geilinger et al. 2020; Hu et al. 2019]. Unlike existing methods that impose equilibrium constraints on explicit triangle or tetrahedron meshes, our formulation enables the solution of inverse problems defined on Voronoi diagrams.

3 DIFFERENTIABLE RESTRICTED VORONOI DIAGRAMS

3.1 Generalized Voronoi Diagrams

The Voronoi cell \mathcal{R}_i for a given site C_i can be defined as

$$\mathcal{R}_i = \{p : d(p, C_i) < d(p, C_j) \forall j \neq i\}, \quad (1)$$

where $d(p, C) = d_{\text{Euclidean}}(p, C)$ is the Euclidean distance between point p and site C . A family of more flexible generalized Voronoi diagrams can be constructed by modifying the distance metric which defines the Voronoi cell.

Mouzarkel [1997] and Eppstein [2012] draw theoretical links between foam structures and generalized Voronoi diagrams, independently showing that a two-dimensional foam at equilibrium is geometrically equivalent to a *sectional multiplicative Voronoi partition* (SMVP),

$$d_{\text{SMVP}}(p, C_i)^2 = \frac{1}{k_i} \left(d_{\text{Euclidean}}(p, C_i)^2 - w_i \right), \quad (2)$$

for some arrangement of sites and weights w, k . The multiplicative weight k gives rise to curved interfaces which, while necessary to represent exact foam structures, significantly complicate computations of geometric properties of cells (Sec. 3.3). Analytic integration over 3D curved surfaces such as soap films is typically impossible,

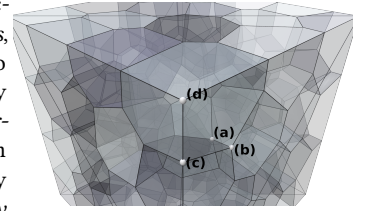
and algebraic line-surface intersection computations, required for boundary clipping, involve solving high-order polynomials even for simple 3D interpolating surfaces. We instead use the power diagram,

$$d_{\text{Power}}(p, C_i)^2 = d_{\text{Euclidean}}(p, C_i)^2 - w_i, \quad (3)$$

for our simulations, which maintains planar interfaces while allowing for cell size variability. Sec. 4.4 demonstrates the power diagram’s capacity to express realistic foam geometry.

3.2 Voronoi Vertices

We compute the restricted Voronoi diagram, constrained to within a bounding domain, as described by Yan *et al.* [2009; 2011]. Each restricted Voronoi vertex in m dimensions is an intersection of m hyperplanes, each of which is either a Voronoi bisector or a facet of the bounding surface. In three dimensions, there are four types of vertices; (a) *unrestricted Voronoi vertices*, *i.e.*, intersections between three (linearly independent) bisectors, (b) *boundary face vertices*, *i.e.*, intersections between two bisectors and one boundary facet, (c) *boundary edge vertices*, *i.e.*, intersections between one bisector and two boundary facets, and (d) *simple boundary vertices*. The generating plane equations can be expressed as simple functions of the input degrees of freedom, *i.e.*, the Voronoi sites and the vertices of the boundary surface. Given as the intersection of three planes, *i.e.*, the solution of a 3×3 linear system, each 3D Voronoi vertex can be expressed in closed-form and differentiated with respect to the inputs.



We derive as an example the closed-form expression for the unrestricted Voronoi vertex in 3D. Given four sites $\mathbf{x}_i = (x_i, y_i, z_i)^T$, $i \in \{0, 1, 2, 3\}$ of a Delaunay simplex, the plane equations of Voronoi bisectors are

$$(x_j - x_i)x + (y_j - y_i)y + (z_j - z_i)z = \frac{1}{2}(x_j^2 - x_i^2 + y_j^2 - y_i^2 + z_j^2 - z_i^2). \quad (4)$$

The intersection $\mathbf{x}_c = (x_c, y_c, z_c)^T$ of three bisectors solves the linear system

$$\begin{bmatrix} x_1 - x_0 & y_1 - y_0 & z_1 - z_0 \\ x_2 - x_0 & y_2 - y_0 & z_2 - z_0 \\ x_3 - x_0 & y_3 - y_0 & z_3 - z_0 \end{bmatrix} \begin{bmatrix} x_c \\ y_c \\ z_c \end{bmatrix} = \frac{1}{2} \begin{bmatrix} x_1^2 - x_0^2 + y_1^2 - y_0^2 + z_1^2 - z_0^2 \\ x_2^2 - x_0^2 + y_2^2 - y_0^2 + z_2^2 - z_0^2 \\ x_3^2 - x_0^2 + y_3^2 - y_0^2 + z_3^2 - z_0^2 \end{bmatrix},$$

for which the solution can be written using the known closed-form expression for the 3×3 matrix inverse. This approach extends to all types of boundary vertices by substituting bisector plane equations in the linear system for plane equations of boundary facets. Furthermore, it is easily adapted for the power diagram by adding $\frac{1}{2}(w_i - w_j)$ to the right hand side of the bisector plane equation (4). In our implementation, code for evaluating these expressions and their derivatives is generated using a computer algebra system.

3.3 Integration over Voronoi Cells

The mechanics of cell-based systems are driven by the energies of individual cells. Cell energies relate to properties such as surface area and volume, which are computed by integrating over the cell geometry. Volume integrals are also used to compute cell centroids

and moments of inertia. Integration over a polyhedral Voronoi cell is performed piecewise by dividing the surface and volume into simplices. A surface integral requires triangulating each facet of the cell and then summing the per-triangle values. A tetrahedralization of the volume is, however, unnecessary for computing volume integrals. Rather, tetrahedra are constructed by joining each surface triangle to the origin as shown in Fig. 2.

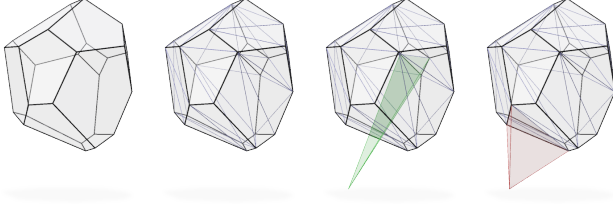


Fig. 2. Volume integration over a 3D Voronoi cell. From left to right: (1) 3D Voronoi cell. (2) Face triangulation. (3) Integration tetrahedron formed by connecting a face triangle to the origin. Tetrahedra can have positive (3) or negative (4) volume.

In addition to avoiding an explicit tetrahedralization, including the origin in each tetrahedron simplifies the simplex integral to a function of three vertices instead of four. Importantly, this reduces the number of first and second derivatives required per simplex. A generic approach for volume integration in these tetrahedra is given in App. A.

3.4 Energy Formulation

We simulate cell mechanics in the implicit Voronoi model by considering a potential energy of the form

$$E = F(\mathbf{c}, \mathbf{x}(\mathbf{c})), \quad (5)$$

where \mathbf{c} is a vector containing the degrees of freedom of all Voronoi sites, and \mathbf{x} is a vector of spatial coordinates of all Voronoi vertices, defined implicitly in terms of \mathbf{c} . In general, an energy depending only on \mathbf{x} is sufficient to describe physical interactions between cells, and explicit dependence on \mathbf{c} is used for regularization. The generic gradient of this energy is

$$\frac{dE}{d\mathbf{c}} = \frac{\partial F}{\partial \mathbf{x}} \frac{d\mathbf{x}}{d\mathbf{c}} + \frac{\partial F}{\partial \mathbf{c}}, \quad (6)$$

and the Hessian follows as

$$\begin{aligned} \frac{d^2E}{d\mathbf{c}^2} &= \left(\frac{d\mathbf{x}}{d\mathbf{c}} \right)^\top \frac{\partial^2 F}{\partial \mathbf{x}^2} \frac{d\mathbf{x}}{d\mathbf{c}} + \left(\frac{d\mathbf{x}}{d\mathbf{c}} \right)^\top \frac{\partial^2 F}{\partial \mathbf{x} \partial \mathbf{c}} \\ &+ \frac{\partial^2 F}{\partial \mathbf{c} \partial \mathbf{x}} \frac{d\mathbf{x}}{d\mathbf{c}} + \sum_i \left(\frac{\partial F}{\partial \mathbf{x}_i} \frac{d^2 \mathbf{x}_i}{d\mathbf{c}^2} \right) + \frac{\partial^2 F}{\partial \mathbf{c}^2}. \end{aligned} \quad (7)$$

This flexible formulation permits any differentiable energy function and is applicable to a wide range of cell-based systems. The same computational method can be used to simulate foam as well as biological tissue, as demonstrated in Sec. 4.

3.5 Boundary Coupling

Many cellular systems interface with external bodies or free space. Biological tissues grow freely or within deformable membranes, while engineering designs that utilize cellular structures must support external loads. To handle these external interactions, we define the bounding domain of the Voronoi diagram by a triangular mesh with vertices $\mathbf{v}(\mathbf{p})$, where \mathbf{p} are boundary degrees of freedom. We let $\mathbf{y} = (\mathbf{c}, \mathbf{p})$ denote the vector holding all degrees of freedom of the coupled system and consider a total potential energy

$$E = F(\mathbf{c}, \mathbf{x}(\mathbf{c}, \mathbf{v}(\mathbf{p}))) + F_B(\mathbf{p}), \quad (8)$$

where F is the potential energy of the cells and F_B is an additional boundary energy which may encode, *e.g.*, the elastic potential of an enclosing membrane. As for the static boundary formulation, we compute the first and second derivatives of the above expression to use in gradient-based optimization. The gradient with respect to \mathbf{p} is given by

$$\frac{dE}{d\mathbf{p}} = \frac{\partial F}{\partial \mathbf{x}} \frac{\partial \mathbf{x}}{\partial \mathbf{v}} \frac{d\mathbf{v}}{d\mathbf{p}} + \frac{dF_B}{d\mathbf{p}}. \quad (9)$$

The additional blocks of the Hessian matrix are given in App. B. This boundary coupling formulation lends extreme flexibility to the model, enabling systems involving elastic membranes, free surfaces, and rigid bodies in addition to fixed boundaries.

3.6 Smoothness

In the general configuration, where each Voronoi vertex in m dimensions is of degree $m + 1$, the topology of the Voronoi diagram is constant within a neighborhood of the given state, and the vertex coordinates \mathbf{x} are a locally smooth function of the Voronoi sites \mathbf{c} . States with higher-degree vertices, which occur during topological transitions, have undefined $\frac{d\mathbf{x}}{d\mathbf{y}}$ which gives rise to non-smooth energies. Cell volume (area in 2D) and other volume integrals of smooth functions are C^1 -continuous across these transitional states, though surface area (perimeter in 2D) is C^0 as noted in [Bogosel and Oudet 2022] for the 2D case.

If cell energy is monotonic in surface area and the domain boundary is convex, the gradient discontinuities are strictly concave, forming local maxima in the energy landscape which do not hinder minimization. Otherwise, the model may fail to converge using such energy functions. Our simulations with non-convex domain boundaries (Secs. 4.1 and 4.3) use C^1 -continuous energies and therefore avoid these problems.

Degenerate configurations exist with lower-order discontinuities, *e.g.* when a parallel boundary facet and Voronoi bisector overlap (discussed in [Liu et al. 2009]) or when multiple Voronoi sites coincide. However, we have not observed these states during simulation and optimization in any of our examples.

3.7 Dynamics

We have so far considered systems at static equilibrium in which the net internal force vanishes,

$$F(\mathbf{y}) = -\frac{dE}{d\mathbf{y}} = \mathbf{0}. \quad (10)$$

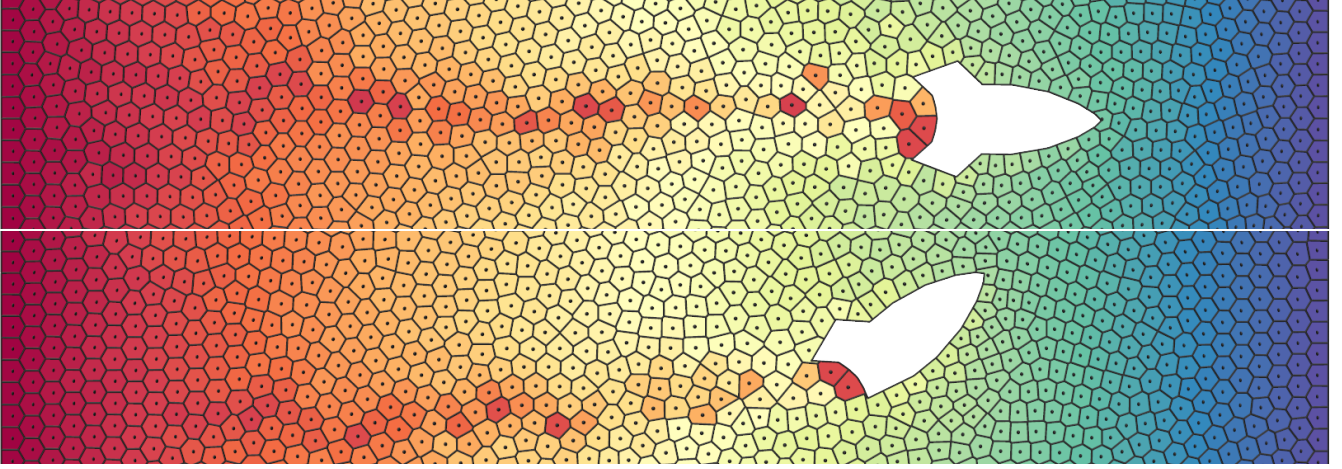


Fig. 3. Two simulations of a rigid body propelled through a tissue-like assembly of elastic Voronoi cells. Cells are colored based on starting position. Turbulence-like effects result in irregular displacement of cells from their starting positions. The asymmetric shape of the second body results in a curved trajectory due to forces from neighboring cells.

We now relax the equilibrium constraint to consider dynamic cell-based systems governed by Newton's second law,

$$F(\mathbf{y}) = \mathbf{M} \frac{d^2 \mathbf{y}}{dt^2}, \quad (11)$$

where \mathbf{M} is a (typically diagonal) mass matrix. We additionally introduce viscous forces $F_f(\mathbf{y}) = -\boldsymbol{\eta} \frac{d\mathbf{y}}{dt}$, where $\boldsymbol{\eta}$ is a diagonal viscosity matrix. The resulting equations of motion are

$$\mathbf{M} \ddot{\mathbf{y}} + \boldsymbol{\eta} \dot{\mathbf{y}} + \frac{dE}{d\mathbf{y}} = \mathbf{0}, \quad (12)$$

where $\dot{\mathbf{y}}$ and $\ddot{\mathbf{y}}$ denote first and second derivatives of \mathbf{y} with respect to time. Unless otherwise noted, we approximate these derivatives using standard finite-differencing, *i.e.*,

$$\begin{aligned} \dot{\mathbf{y}} &\approx \frac{1}{h} (\mathbf{y}_{k+1} - \mathbf{y}_k), \\ \ddot{\mathbf{y}} &\approx \frac{1}{h^2} (\mathbf{y}_{k+1} - 2\mathbf{y}_k + \mathbf{y}_{k-1}). \end{aligned} \quad (13)$$

If the energy function is at least C^1 -continuous, quadratic convergence can be achieved using a second-order discretization (BDF2) for the accelerations,

$$\ddot{\mathbf{y}} \approx \frac{1}{2h^2} (3\mathbf{y}_{k+1} - 7\mathbf{y}_k + 5\mathbf{y}_{k-1} - \mathbf{y}_{k-2}). \quad (14)$$

Evidence of quadratic convergence under refinement of the simulation time step is shown in App. C. The equations of motion can be solved for the next state \mathbf{y}_{k+1} via the optimization problem

$$\mathbf{y}_{k+1} = \operatorname{argmin}_{\mathbf{y}} \frac{a_2}{2} \ddot{\mathbf{y}}^\top \mathbf{M} \ddot{\mathbf{y}} + \frac{a_1}{2} \dot{\mathbf{y}}^\top \boldsymbol{\eta} \dot{\mathbf{y}} + E(\mathbf{y}), \quad (15)$$

where a_1, a_2 are the \mathbf{y}_{k+1} -coefficients of the first and second finite-difference derivatives. Many cell-based systems operate at low Reynolds numbers, where inertia is dominated by viscous effects. For such cases, the momentum term can be neglected, leaving

$$\mathbf{y}_{k+1} = \operatorname{argmin}_{\mathbf{y}} \frac{a_1}{2} \dot{\mathbf{y}}^\top \boldsymbol{\eta} \dot{\mathbf{y}} + E(\mathbf{y}). \quad (16)$$

3.8 Equilibrium-Constrained Optimization

In addition to forward simulation, our approach can be extended to solve inverse simulation tasks formulated as equilibrium-constrained optimization problems. The goal is then to find optimal parameter values for a cell-based system such that the corresponding equilibrium state best satisfies a given objective. We demonstrate in Sec. 4.4 that this framework is useful for characterizing real-world cell-based systems from images.

A general equilibrium-constrained optimization problem reads

$$\min_{\mathbf{y}, \mathbf{u}} L(\mathbf{y}, \mathbf{u}) \quad \text{s.t.} \quad \frac{\partial}{\partial \mathbf{y}} E(\mathbf{y}, \mathbf{u}) = \mathbf{0}, \quad (17)$$

where L is an objective function, \mathbf{y} are dynamic degrees of freedom, and \mathbf{u} are optimization variables. The system is constrained to be at equilibrium, hence the state \mathbf{y} is a function of \mathbf{u} . The gradient is given by

$$\frac{dL}{d\mathbf{u}} = \frac{\partial L}{\partial \mathbf{y}} \frac{d\mathbf{y}}{d\mathbf{u}} + \frac{\partial L}{\partial \mathbf{u}}, \quad (18)$$

where the simulation derivatives $\frac{d\mathbf{y}}{d\mathbf{u}}$ can be computed using the implicit function theorem,

$$\frac{d}{d\mathbf{u}} \frac{\partial}{\partial \mathbf{y}} E(\mathbf{y}, \mathbf{u}) = \mathbf{0} \rightarrow \frac{d\mathbf{y}}{d\mathbf{u}} = - \left(\frac{\partial^2 E}{\partial \mathbf{y}^2} \right)^{-1} \frac{\partial^2 E}{\partial \mathbf{y} \partial \mathbf{u}}. \quad (19)$$

Having evaluated the objective gradient with respect to the optimization variables \mathbf{u} , we can minimize the L using first-order or quasi-Newton methods. Whenever the optimization parameters are updated during this process, we recompute the equilibrium state $\mathbf{y}(\mathbf{u})$ and ensure monotonic decrease of the objective using a backtracking line search.

3.9 Implementation

The method is implemented in C++ using the Eigen library [Guennebaud et al. 2010] for matrix and vector operations, and the CHOLMOD

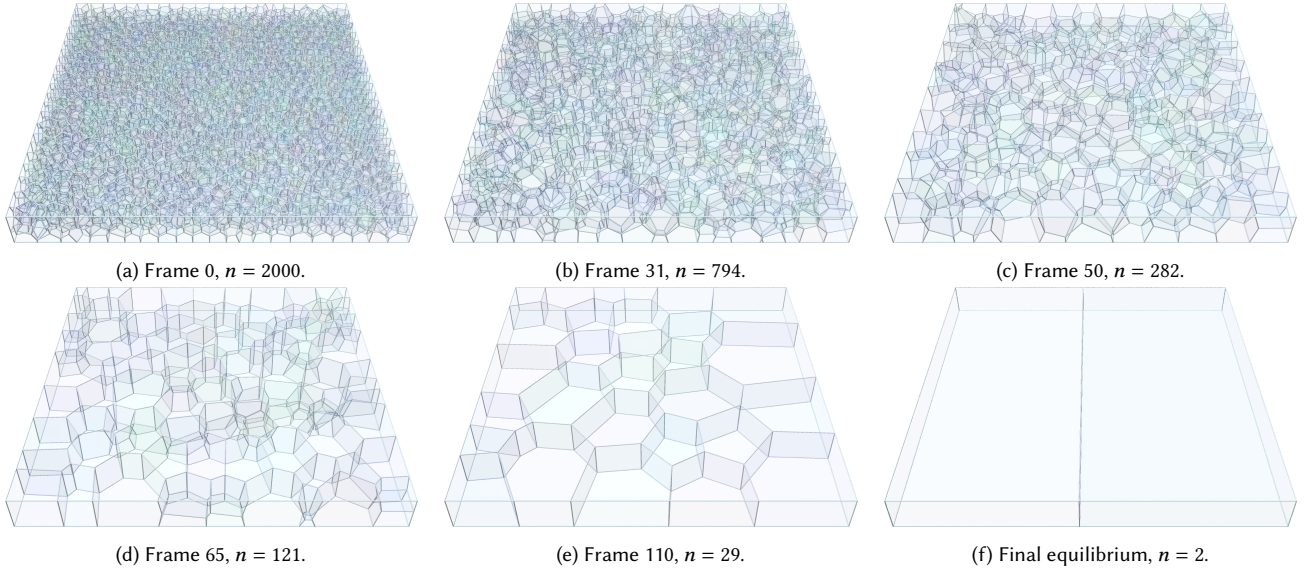


Fig. 4. Coarsening of an initially monodisperse dry foam in a flattened box. 2000 cells collapse to a two-cell equilibrium in 350 frames.

solver [Chen et al. 2008] for linear systems. Geometry processing libraries CGAL [Yvinec 2023] and Geogram [Lévy 2015] are used in Voronoi diagram generation. Finally, we use Polyscope [Sharp et al. 2019] for visualization and rendering of figures. Our code can be found at <https://github.com/lnumerow-ethz/VoronoiCellSim>.

4 RESULTS

4.1 Intercellular Navigation with Rigid Body

In this first 2D experiment, we simulate the propulsion of a rigid body through a tissue-like assembly of elastic Voronoi cells. The cell energy is given by

$$E = a_0(A - \bar{A})^2 + a_1 \int_{x \in R} \|x - \bar{x}\|^2 dA + a_2 \|c - \bar{x}\|^2, \quad (20)$$

where A and \bar{A} are the current and target area of the cell, \bar{x} is its centroid, and c is the Voronoi site position. In this and the following examples, the final term is a regularizer on the distance between the site and its cell centroid. The rigid body, modelled as an internal clipping geometry with translation and rotation degrees of freedom (see Sec. 3.5), is subject to a constant force F_x to the right. We use a dynamics model with momentum (Eq. 15) to resolve turbulence-like effects in the system, the results of which can be observed in Fig. 3. The curved trajectory of the rigid body in the second example is a result of its asymmetric shape and forces applied by the surrounding cells. This demonstrates the dynamic coupling between the cells and boundary degrees of freedom.

For this and the following experiments, refer to App. D for parameter values and additional details for reproducibility.

4.2 Foam Coarsening

Due to pressure differences between bubbles in an equilibrated liquid foam, gas diffuses slowly through the interfaces from smaller, higher-pressure bubbles into larger, lower-pressure ones. As a result,

smaller foam cells collapse and the total number of foam cells in the system decreases over time in a process known as *coarsening*. This phenomenon has seen extensive research [Thomas et al. 2015; Vedel-Larsen 2010] due to its detrimental effect in applications such as enhanced oil recovery. Foam coarsening presents a challenge for vertex models due to the topological changes which result from the collapse and removal of a cell, particularly in 3D. Existing 2D vertex models [Vedel-Larsen 2010] rely on heuristics to remove collapsing cells and reconstruct topology, resulting in discontinuous changes to neighboring cell volumes and to the system energy.

We simulate dry foam coarsening using a momentumless dynamic model as described in Eq. 16. Each site has five degrees of freedom: three spatial coordinates (x, y, z) , a power diagram weight w and a volume target \bar{V} representing the mass of air contained in the cell. The energy of a cell is

$$E = a_0 \left(\frac{V}{\bar{V}} - 1 \right)^2 + a_1 A + a_2 \|c - \bar{x}\|^2, \quad (21)$$

where V and A are the volume and surface area, \bar{x} is the centroid and c is the Voronoi site position. The viscosity coefficients (diagonal entries of $\boldsymbol{\eta}$ in Eq. (16)) of the site degrees of freedom are very small, such that the system evolves quasi-statically. The larger viscosity coefficient, corresponding to the volume target \bar{V} , represents the resistance to diffusion of air through the foam interfaces. Fig. 4 shows the result of a large-scale 3D coarsening simulation beginning with $n = 2000$ monodisperse foam cells. Variation of power diagram weights in our differentiable Voronoi model allows cells to collapse smoothly to zero volume. Furthermore, our model implicitly performs the complete topological restructuring of the local neighborhood that results from each cell collapse. It should be noted that the geometric accuracy of this simulation, and other foam simulations involving wide variation of cell sizes and pressures, is limited due to the lack of curved interfaces.

4.3 Biological Tissue Growth

Embryonic *cleavage* is the process in which a complex organism grows from a single cell via repeated cell division. It involves an exponential increase in the number of cells and therefore a rapid increase in the complexity of an organism. Cell *proliferation*, a similar process that involves the growth and subsequent division of cells, is another primary driver of tissue development. Simulation of such processes is a common use case for computational models [Conradin et al. 2021; Ghaffarizadeh et al. 2018]. Our first experiment simulates embryonic cleavage in a spherical membrane, beginning with a single Voronoi cell. By the dynamic coupling formulation described in Sec. 3.5, the domain boundary is deformable and subject to its own elastic forces, with a boundary mesh edge of length ℓ having energy $E_B = k\ell^2$. The cell energy is

$$E = a_0 \left(\frac{V}{\bar{V}} - 1 \right)^2 + \frac{a_1}{\bar{V}^{4/3}} \int_{x \in \mathcal{R}} \|x - \bar{x}\|^2 dV + \frac{a_2}{\bar{V}^{2/3}} \|c - \bar{x}\|^2, \quad (22)$$

where V and \bar{V} are the current and rest volumes, \bar{x} is the centroid and c is the Voronoi site position. We simulate the evolution of the system using a momentumless dynamic model as described in Eq. (16). After every k simulation time steps, each Voronoi site is replaced by two daughter sites at positions $c \pm \beta \bar{V}^{1/3} \mathbf{n}$, where \mathbf{n} is the unit normal vector to the cleavage plane. The first three cleavages are orthogonal, after which the cleavage planes are chosen randomly. The daughter sites are initialized with the same power diagram weight as the parent site, and rest volume $\frac{1}{2} \bar{V}_{\text{parent}}$. The system is simulated over 700 time steps with a division every $T = 60$ frames, resulting in a final cell count of 4096. In Fig. 1, the simulated embryo is compared to frames from [van Ijken 2018] depicting embryonic development of a salamander. While this comparison is not intended to be quantitative, it shows that our method is able to produce simulations qualitatively similar to real-world cellular systems undergoing many topological changes.

A second experiment simulates cell proliferation in a cylindrical container of radius 1, with an added gravity term and free upper surface (Fig. 5). After each simulation step of size h , each cell divides with probability $p = \alpha \bar{V} h$, where α is the proliferation rate of the tissue. The daughter sites are initialized with rest volume $\frac{1}{2} \bar{V}_{\text{parent}}$ increasing linearly to $\gamma \bar{V}_{\text{parent}}$ over time period τ .

4.4 Characterization of Foam from Image

We apply our equilibrium-constrained optimization formulation (Sec. 3.8) to characterize a 2D foam from an image and create a matching computational model. The image (Fig. 6a) was taken in our lab and depicts a soap foam between two glass plates. We manually annotate the image, defining the vertex coordinates and the edges in the desired tessellation. We assume a cell energy of the form

$$E = a_0 (A - \bar{A})^2 + a_1 P, \quad (23)$$

where A and P are the cell area and perimeter, and \bar{A} is a target area. This is analogous to the 3D dry foam energy used in our coarsening simulation (Sec. 4.2). The model is initialized by placing sites at the centroids of the cells in the annotated image, and assigning \bar{A} equal to their area. The system is allowed to converge to equilibrium, resulting in the pre-optimization model shown in Fig. 6b. We then

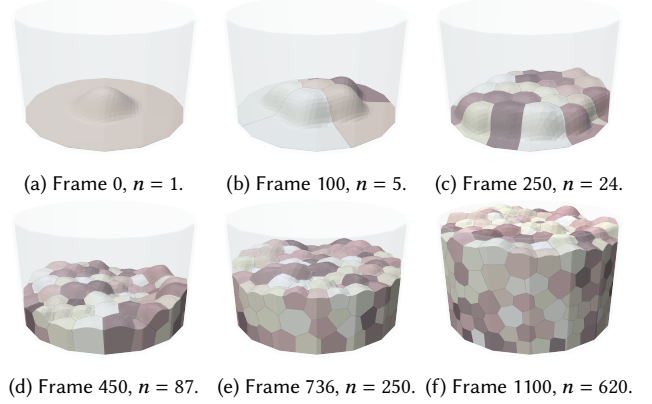


Fig. 5. Cell proliferation in a cylindrical container. The free boundary is coupled to the cells using a weak elastic membrane model. Random cell divisions induce frequent and irregular topology changes throughout the simulation.

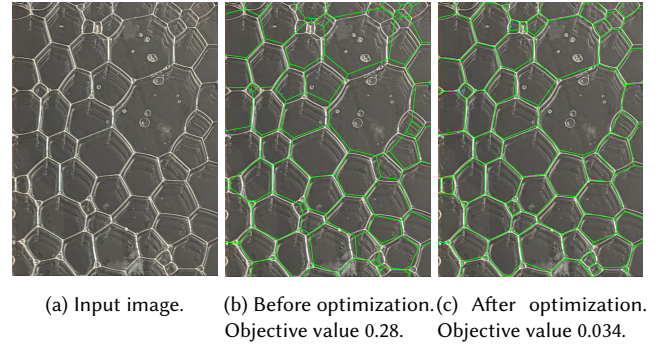


Fig. 6. Construction of a Voronoi foam model from an input image using equilibrium-constrained optimization.

perform equilibrium-constrained optimization on the area targets \bar{A} to find cell pressures matching the observed configuration. The optimization objective is to minimize the sum of squared distances between the annotation vertices and the corresponding Voronoi vertices. The corresponding Voronoi vertex does not need to exist in the tessellation; the generating expression (the circumcenter of the three neighboring sites, or similar for boundary vertices) is always computable. The optimization converged in 77 L-BFGS iterations and 13 seconds of computation time. As can be seen from Fig. 6c, the optimization successfully reduces the discrepancy between simulated and real-world foams. It should be noted that this procedure converges reliably to a good solution only when the topology of the initial equilibrium state matches that in the image.

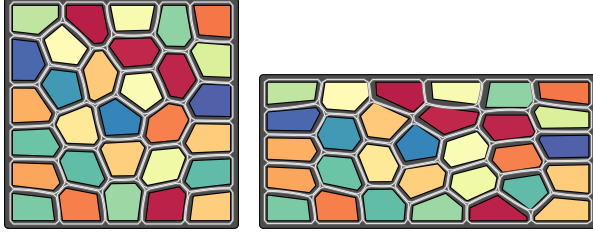
4.5 Comparison to Deformable Cell Model

To compare the accuracy and performance of our model with other simulation methods, we construct a deformable cell model (DCM) using Incremental Potential Contact (IPC) [Li et al. 2020] to resolve contact between the cells. The DCM cells have 30 vertices and hence 60 degrees of freedom, while ours are power diagram cells with 3

degrees of freedom. We use a per-cell energy of the form

$$E = a_0(A - \bar{A})^2 + a_1P^2, \quad (24)$$

where A and P are the cell area and perimeter, and \bar{A} is a target area. We use a combined target of 1.2 times the domain area such that the DCM cells are in compression and fill the entire space. The DCM uses an additional quadratic penalty per edge length for regularization as well as the IPC energy. We perform a quasi-static



(a) Initial state, 1x1 domain. (b) Final state, 1.50x0.67 domain.

simulation with 30 cells starting in a square domain. The initial state for the DCM is constructed by offsetting each Voronoi cell inward and distributing vertices evenly around the perimeter, followed by energy minimization to reach equilibrium. In each frame, the domain is reshaped and both models are allowed to converge to a new equilibrium. The two models behave similarly, achieving the same final topology as shown in Fig. 7. However, the DCM required 1000 times more computation time and nearly 40 times as many average Newton iterations to converge (see Table 1), demonstrating the efficiency of our implicit Voronoi model.

simulation with 30 cells starting in a square domain. The initial state for the DCM is constructed by offsetting each Voronoi cell inward and distributing vertices evenly around the perimeter, followed by energy minimization to reach equilibrium. In each frame, the domain is reshaped and both models are allowed to converge to a new equilibrium. The two models behave similarly, achieving the same final topology as shown in Fig. 7. However, the DCM required 1000 times more computation time and nearly 40 times as many average Newton iterations to converge (see Table 1), demonstrating the efficiency of our implicit Voronoi model.

4.6 Runtime

Runtime statistics for all simulation experiments are collected in Table 1. Experiments are performed using a workstation with an AMD Ryzen Threadripper PRO 5995WX CPU.

The number of iterations per frame depends highly on the number and complexity of topological changes that occur, resulting in large discrepancies among the 3D experiments. In the embryonic cleavage example, few topological changes occur except in the frames immediately following each simultaneous cell division. The coarsening example is particularly expensive because many cells collapse per frame, and cell collapse results in more complex topological changes than intercalation. Furthermore, the energy gradient in the coarsening example is discontinuous across topology changes, slowing the convergence of Newton’s method, while the other examples use C^1 -continuous energies.

We perform an additional experiment to measure the runtime scaling of our method with number of cells. In a square (2D) or cube (3D) with n randomly placed Voronoi sites, we perform a single Newton iteration and measure the total runtime, along with the runtime of significant subroutines including the generation of the Voronoi diagram, computation of the energy Hessian and solution

of the linear system (Fig. 8). As can be observed from the results,

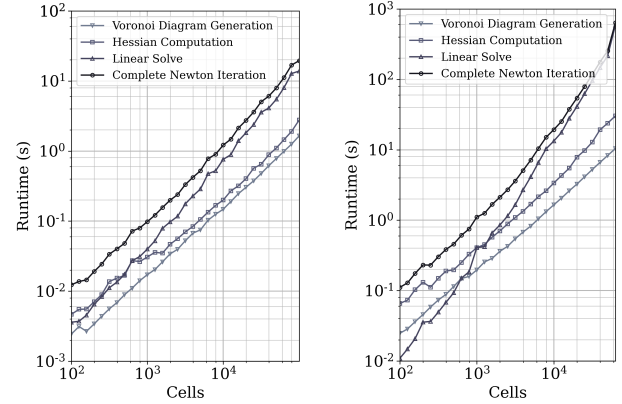


Fig. 8. Runtime of a Newton iteration vs. number of cells for 2D (left) and 3D (right) models. In the range of problem sizes considered, the Voronoi diagram generation (including evaluation of derivatives e.g. $\frac{dx}{dc}$) and Hessian computation exhibit roughly linear scaling, while the cost of solving the linear system dominates for larger problems.

3D cases are significantly more expensive than 2D cases for similar numbers of cells. This is primarily due to the increase in average number of neighbors for each cell, from 6 in 2D to ~ 15.5 [Meijering 1953] in 3D, leading to a much denser Hessian and a larger number of Voronoi vertices.

5 CONCLUSIONS

We have proposed a novel simulation approach for mechanical cellular systems based on differentiable Voronoi diagrams. The method successfully addresses challenges faced by existing models in handling topological transitions, while using an extremely compact state representation that implicitly defines the shape and topology of the interface network. We demonstrated this using a diverse set of examples, including simulations of complex biological and physical processes as well as comparisons to alternative models and real-world systems.

5.1 Limitations & Future Work

The development of informative biological simulations will require more complex energy models and the incorporation of real-world data to determine accurate parameters. Deriving a smoother approximation to the surface area of Voronoi cells would enable further applications, including adhesion effects at biological cell interfaces. Our model currently uses an isotropic distance metric that restricts the space of possible cell shapes, and the method assumes planar or piecewise linear cell interfaces. However, epithelial tissues, for example, exhibit non-convex scutoid-shaped cells [Gómez-Gálvez et al. 2018] which permit different cell packing patterns. Extending our method towards more complex cell shapes while retaining a compact site-based representation is an interesting challenge for future work. Voronoi diagrams are also a natural design space for foam-like 3D-printed metamaterials. This direction has been explored, e.g., by Martinez et al. [2018], with extensions to orthotropic foams based on

Table 1. Runtime statistics for experiments. Each frame represents one simulation time step and consists of solving a single optimization problem.

Experiment	# Cells	# DOF	# Frames	# Iter / Frame (avg / max)	Time / Iter (avg) [ms]	Total time [s]
Comparison (Ours)	30	90	100	5/25	2.32	1.23
Comparison (DCM)	30	1800	100	195/2621	65	1258
Tissue Growth (membrane)	4096	24070	700	3/12	3830	8521
Tissue Growth (cylinder)	620	6067	1101	10/47	1383	14970
Coarsening	2000	10000	350	51/522	1275	22996
Rigid Body 1	2000	4003	396	3/4	212	251
Rigid Body 2	2000	4003	304	3/5	213	194

Voronoi diagrams with spatially varying distance metrics [Martinez et al. 2019]. An extension of our approach may permit gradient-based optimization of these materials. Finally, we have investigated a simple instance of intercellular navigation, where a rigid object is driven by a constant force. Designing control algorithms to guide an object through cellular systems towards a desired target is another exciting future direction.

ACKNOWLEDGMENTS

We thank the anonymous reviewers for their valuable feedback. This work was supported by the European Research Council (ERC) under the European Union’s Horizon 2020 research and innovation program (grant agreement No. 866480), and the Swiss National Science Foundation through SNF project grant 200021_200644.

REFERENCES

Silvanus Alt, Poulami Ganguly, and Guillaume Salbreux. 2017. Vertex models: From cell mechanics to tissue morphogenesis. *Philosophical Transactions of the Royal Society B: Biological Sciences* 372 (05 2017), 20150520. <https://doi.org/10.1098/rstb.2015.0520>

Adam W. Bargteil, Chris Wojtan, Jessica K. Hodgins, and Greg Turk. 2007. A finite element method for animating large viscoplastic flow. In *ACM SIGGRAPH 2007 Papers* (San Diego, California) (SIGGRAPH '07). Association for Computing Machinery, New York, NY, USA, 16–es. <https://doi.org/10.1145/1275808.1276397>

Bernd Bickel, Moritz Bächer, Miguel A. Otaduy, Wojciech Matusik, Hanspeter Pfister, and Markus Gross. 2009. Capture and modeling of non-linear heterogeneous soft tissue. *ACM Trans. Graph.* 28, 3, Article 89 (jul 2009), 9 pages. <https://doi.org/10.1145/1531326.1531395>

Benjamin Bogosel and Edouard Oudet. 2022. Longest minimal length partitions. *Interfaces and Free Boundaries* 24, 1 (Jan. 2022), 95–135. <https://doi.org/10.4171/IFB/468>

Tyson Brochu and Robert Bridson. 2009. Robust Topological Operations for Dynamic Explicit Surfaces. *SIAM J. Sci. Comput.* 31, 4 (jun 2009), 2472–2493. <https://doi.org/10.1137/080737617>

G. Wayne Brodland, Daniel I-Li Chen, and Jim H. Veldhuis. 2006. A cell-based constitutive model for embryonic epithelia and other planar aggregates of biological cells. *International Journal of Plasticity* 22, 6 (2006), 965–995. <https://doi.org/10.1016/j.ijplas.2005.05.002>

Oleksiy Busaryev, Tamal K. Dey, Huamin Wang, and Zhong Ren. 2012. Animating Bubble Interactions in a Liquid Foam. *ACM Trans. Graph.* 31, 4, Article 63 (jul 2012), 8 pages. <https://doi.org/10.1145/2185520.2185559>

Xiang Chen, Changxi Zheng, Weiwei Xu, and Kun Zhou. 2014. An asymptotic numerical method for inverse elastic shape design. *ACM Trans. Graph.* 33, 4, Article 95 (jul 2014), 11 pages. <https://doi.org/10.1145/2601097.2601189>

Yanqing Chen, Timothy A Davis, William W Hager, and Sivasankaran Rajamanickam. 2008. Algorithm 887: CHOLMOD, supernodal sparse Cholesky factorization and update/downdate. *ACM Transactions on Mathematical Software (TOMS)* 35, 3 (2008), 1–14.

Raphaël Conradin, Christophe Coreixas, Jonas Latt, and Bastien Chopard. 2021. Pala-Cell2D: A framework for detailed tissue morphogenesis. *Journal of Computational Science* 53 (2021), 101353. <https://doi.org/10.1016/j.jocs.2021.101353>

Fang Da, Christopher Batty, Chris Wojtan, and Eitan Grinspun. 2015. Double Bubbles Sans Toil and Trouble: Discrete Circulation-Preserving Vortex Sheets for Soap Films and Foams. *ACM Trans. on Graphics (SIGGRAPH North America 2015)* (2015).

Fernando de Goes, Corentin Wallez, Jin Huang, Dmitry Pavlov, and Mathieu Desbrun. 2015. Power Particles: An Incompressible Fluid Solver Based on Power Diagrams. *ACM Trans. Graph.* 34, 4, Article 50 (jul 2015), 11 pages. <https://doi.org/10.1145/2766901>

Yitong Deng, Mengdi Wang, Xiangxin Kong, Shiyong Xiong, Zangyueyang Xian, and Bo Zhu. 2022. A moving eulerian-lagrangian particle method for thin film and foam simulation. *ACM Trans. Graph.* 41, 4, Article 154 (jul 2022), 17 pages. <https://doi.org/10.1145/3528223.3530174>

David Eppstein. 2012. The Graphs of Planar Soap Bubbles. <https://doi.org/10.48550/ARXIV.1207.3761>

Reza Farhadifar, Jens-Christian Röper, Benoit Aigouy, Suzanne Eaton, and Frank Jülicher. 2007. The Influence of Cell Mechanics, Cell-Cell Interactions, and Proliferation on Epithelial Packing. *Current Biology* 17, 24 (2007), 2095–2104. <https://doi.org/10.1016/j.cub.2007.11.049>

Fan Feng, Shiyong Xiong, Ziyue Liu, Zangyueyang Xian, Yuqing Zhou, Hiroki Kobayashi, Atsushi Kawamoto, Tsuyoshi Nomura, and Bo Zhu. 2022. Cellular topology optimization on differentiable Voronoi diagrams. *Internat. J. Numer. Methods Engrg.* 124, 1 (sep 2022), 282–304. <https://doi.org/10.1002/nme.7121>

Zachary Ferguson, Teseo Schneider, Danny Kaufman, and Daniele Panozzo. 2023. In-Timestep Remeshing for Contacting Elastodynamics. *ACM Trans. Graph.* 42, 4, Article 145 (jul 2023), 15 pages. <https://doi.org/10.1145/3592428>

Alexander G. Fletcher, Miriam Osterfield, Ruth E. Baker, and Stanislav Y. Shvartsman. 2014. Vertex Models of Epithelial Morphogenesis. *Biophysical Journal* 106, 11 (2014), 2291–2304. <https://doi.org/10.1016/j.bpj.2013.11.4498>

Moritz Geilinger, David Hahn, Jonas Zehnder, Moritz Bächer, Bernhard Thomaszewski, and Stelian Coros. 2020. Add: Analytically differentiable dynamics for multi-body systems with frictional contact. *ACM Transactions on Graphics (TOG)* 39, 6 (2020), 1–15.

Ahmadreza Ghaffarizadeh, Randy Heiland, Samuel H. Friedman, Shannon M. Mumenthaler, and Paul Macklin. 2018. PhysiCell: An open source physics-based cell simulator for 3-D multicellular systems. *PLoS Computational Biology* 14, 2 (02 2018), 1–31. <https://doi.org/10.1371/journal.pcbi.1005991>

Ryan Goldade, Mridul Aanjaneya, and Christopher Batty. 2020. Constraint bubbles and affine regions: reduced fluid models for efficient immersed bubbles and flexible spatial coarsening. *ACM Trans. Graph.* 39, 4, Article 43 (aug 2020), 15 pages. <https://doi.org/10.1145/3386569.3392455>

Pedro Gómez-Gálvez, Pablo Vicente-Munuera, Antonio Tagua, Cristina Forja, Ana M Castro, Marta Letrán, Andrea Valencia-Expósito, Clara Grima, Marina Bermúdez-Gallardo, Óscar Serrano-Pérez-Higueras, et al. 2018. Scutoids are a geometrical solution to three-dimensional packing of epithelia. *Nature communications* 9, 1 (2018), 2960.

Gaël Guennebaud, Benoît Jacob, et al. 2010. Eigen v3. <http://eigen.tuxfamily.org>.

David Hahn, Pol Banzet, James M Bern, and Stelian Coros. 2019. Real2sim: Visco-elastic parameter estimation from dynamic motion. *ACM Transactions on Graphics (TOG)* 38, 6 (2019), 1–13.

Hisao Honda, Masaharu Tanemura, and Tatsuzo Nagai. 2004. A three-dimensional vertex dynamics cell model of space-filling polyhedra simulating cell behavior in a cell aggregate. *Journal of Theoretical Biology* 226, 4 (2004), 439–453. <https://doi.org/10.1016/j.jtbi.2003.10.001>

Jeong-Mo Hong, Ho-Young Lee, Jong-Chul Yoon, and Chang-Hun Kim. 2008. Bubbles alive. *ACM Trans. Graph.* 27, 3 (aug 2008), 1–4. <https://doi.org/10.1145/1360612.1360647>

Yuanming Hu, Jiancheng Liu, Andrew Spielberg, Joshua B Tenenbaum, William T Freeman, Jiajun Wu, Daniela Rus, and Wojciech Matusik. 2019. Chainqueen: A real-time differentiable physical simulator for soft robotics. In *2019 International conference on robotics and automation (ICRA)*. IEEE, 6265–6271.

Weizhen Huang, Julian Iseringhausen, Tom Kneiphof, Ziyin Qu, Chenfanfu Jiang, and Matthias B. Hüllin. 2020. Chemomechanical simulation of soap film flow

- on spherical bubbles. *ACM Trans. Graph.* 39, 4, Article 41 (aug 2020), 14 pages. <https://doi.org/10.1145/3386569.3392094>
- Sadashige Ishida, Peter Synak, Fumiya Narita, Toshiya Hachisuka, and Chris Wojtan. 2020. A model for soap film dynamics with evolving thickness. *ACM Trans. Graph.* 39, 4, Article 31 (aug 2020), 11 pages. <https://doi.org/10.1145/3386569.3392405>
- Sangwoo Kim, Marie Pochitaloff, Georgina Stooke-Vaughan, and Otger Campàs. 2021. Embryonic Tissues as Active Foams. *Nature Physics* 17 (07 2021), 1–8. <https://doi.org/10.1038/s41567-021-01215-1>
- Yohei Kondo, Kazuhiro Aoki, and Shin Ishii. 2018. Inverse tissue mechanics of cell monolayer expansion. *PLoS Computational Biology* 14 (03 2018), e1006029. <https://doi.org/10.1371/journal.pcbi.1006029>
- Dan Koschier, Sebastian Lipponer, and Jan Bender. 2014. Adaptive Tetrahedral Meshes for Brittle Fracture Simulation. In *Symposium on Computer Animation*, Vol. 3. Bruno Lévy. 2015. Geogram. <https://github.com/BrunoLévy/geogram>.
- Minchen Li, Zachary Ferguson, Teseo Schneider, Timothy Langlois, Denis Zorin, Daniele Panozzo, Chenfanfu Jiang, and Danny M. Kaufman. 2020. Incremental Potential Contact: Intersection-and Inversion-Free, Large-Deformation Dynamics. *ACM Trans. Graph.* 39, 4, Article 49 (aug 2020), 20 pages. <https://doi.org/10.1145/3386569.3392425>
- Yang Liu, Wenping Wang, Bruno Lévy, Feng Sun, Dong-Ming Yan, Lin Lu, and Chenglei Yang. 2009. On Centroidal Voronoi Tessellation—Energy Smoothness and Fast Computation. *ACM Trans. Graph.* 28, 4, Article 101 (sep 2009), 17 pages. <https://doi.org/10.1145/1559755.1559758>
- S. Lloyd. 1982. Least squares quantization in PCM. *IEEE Transactions on Information Theory* 28, 2 (1982), 129–137. <https://doi.org/10.1109/TIT.1982.1056489>
- Thomas S Lumpe, Michael Tao, Kristina Shea, and David I W Levin. 2022. Computational design and fabrication of active 3D-printed multi-state structures for shape morphing. *Smart Materials and Structures* 32, 1 (dec 2022), 015008. <https://doi.org/10.1088/1361-665X/aca5d6>
- Mickaël Ly, Romain Casati, Florence Bertails-Descoubes, Mélina Skouras, and Laurence Boissieux. 2018. Inverse elastic shell design with contact and friction. *ACM Trans. Graph.* 37, 6, Article 201 (dec 2018), 16 pages. <https://doi.org/10.1145/3272127.3275036>
- Jonàs Martínez, Samuel Hornus, Haichuan Song, and Sylvain Lefebvre. 2018. Polyhedral Voronoi Diagrams for Additive Manufacturing. *ACM Trans. Graph.* 37, 4, Article 129 (jul 2018), 15 pages. <https://doi.org/10.1145/3197517.3201343>
- Jonàs Martínez, Mélina Skouras, Christian Schumacher, Samuel Hornus, Sylvain Lefebvre, and Bernhard Thomaszewski. 2019. Star-Shaped Metrics for Mechanical Metamaterial Design. *ACM Trans. Graph.* 38, 4, Article 82 (jul 2019), 13 pages. <https://doi.org/10.1145/3306346.3322989>
- J. L. Meijering. 1953. Interface area, edge length, and number of vertices in crystal aggregates with random nucleation. *Philips Research Reports* 8 (1953), 270–290.
- E. Miguel, D. Bradley, B. Thomaszewski, B. Bickel, W. Matusik, M. A. Otaduy, and S. Marschner. 2012. Data-Driven Estimation of Cloth Simulation Models. *Comput. Graph. Forum* 31, 2pt2 (may 2012), 519–528.
- Marek K. Misztal, Kenny Erleben, Adam Bargteil, Jens Fursund, Brian Bunch Christensen, J. Andreas Bærentzen, and Robert Bridson. 2014. Multiphase Flow of Immiscible Fluids on Unstructured Moving Meshes. *IEEE Transactions on Visualization and Computer Graphics* 20, 1 (jan 2014), 4–16. <https://doi.org/10.1109/TVCG.2013.97>
- Juan Montes, Bernhard Thomaszewski, Sudhir Mudur, and Tiberiu Popa. 2020. Computational design of skintight clothing. *ACM Trans. Graph.* 39, 4, Article 105 (aug 2020), 12 pages. <https://doi.org/10.1145/3386569.3392477>
- C. Moukarzel. 1997. Geometrical consequences of foam equilibrium. *Phys. Rev. E* 55 (jun 1997), 6866–6880. Issue 6. <https://doi.org/10.1103/PhysRevE.55.6866>
- Rahul Narain, Tobias Pfaff, and James F. O’Brien. 2013. Folding and crumpling adaptive sheets. *ACM Trans. Graph.* 32, 4, Article 51 (jul 2013), 8 pages. <https://doi.org/10.1145/2461912.2462010>
- Rahul Narain, Armin Samii, and James F. O’Brien. 2012. Adaptive anisotropic remeshing for cloth simulation. *ACM Trans. Graph.* 31, 6, Article 152 (nov 2012), 10 pages. <https://doi.org/10.1145/2366145.2366171>
- James F. O’Brien, Adam W. Bargteil, and Jessica K. Hodgins. 2002. Graphical modeling and animation of ductile fracture. *ACM Trans. Graph.* 21, 3 (jul 2002), 291–294. <https://doi.org/10.1145/566654.566579>
- Satoru Okuda, Yasuhiro Inoue, Mototsugu Eiraku, Yoshiki Sasai, and Taiji Adachi. 2012. Reversible network reconnection model for simulating large deformation in dynamic tissue morphogenesis. *Biomechanics and modeling in mechanobiology* 12 (09 2012). <https://doi.org/10.1007/s10237-012-0430-7>
- Julian Panetta, Florin Isvoranu, Tian Chen, Emmanuel Siefert, Benoit Roman, and Mark Pauly. 2021. Computational Inverse Design of Surface-Based Inflatables. *ACM Trans. Graph.* 40, 4, Article 40 (July 2021), 14 pages. <https://doi.org/10.1145/3450626.3459789>
- Julian Panetta, Abtin Rahimian, and Denis Zorin. 2017. Worst-case stress relief for microstructures. *ACM Trans. Graph.* 36, 4, Article 122 (jul 2017), 16 pages. <https://doi.org/10.1145/3072959.3073649>
- Tobias Pfaff, Rahul Narain, Juan Miguel de Joya, and James F. O’Brien. 2014. Adaptive tearing and cracking of thin sheets. *ACM Trans. Graph.* 33, 4, Article 110 (jul 2014), 9 pages. <https://doi.org/10.1145/2601097.2601132>
- Andrey Piatnitski and Mariya Ptashnyk. 2020. Homogenization of biomechanical models of plant tissues with randomly distributed cells. *Nonlinearity* 33 (09 2020), 5510–5542. <https://doi.org/10.1088/1361-6544/ab95ab>
- Camille Schreck, Damien Rohmer, Stefanie Hahmann, Marie-Paule Cani, Shuo Jin, Charlie C. L. Wang, and Jean-François Bloch. 2016. Nonsmooth Developable Geometry for Interactively Animating Paper Crumpling. *ACM Trans. Graph.* 35, 1, Article 10 (dec 2016), 18 pages. <https://doi.org/10.1145/2829948>
- Nicholas Sharp et al. 2019. Polyscope. www.polyscope.run.
- Mélina Skouras, Bernhard Thomaszewski, Peter Kaufmann, Akash Garg, Bernd Bickel, Eitan Grinspun, and Markus Gross. 2014. Designing inflatable structures. *ACM Trans. Graph.* 33, 4, Article 63 (jul 2014), 10 pages. <https://doi.org/10.1145/2601097.2601166>
- Gilberto Thomas, Julio Belmonte, François Graner, James Glazier, and Rita de Almeida. 2015. 3D simulations of wet foam coarsening evidence a self similar growth regime. *Colloids and Surfaces A: Physicochemical and Engineering Aspects* 473 (02 2015). <https://doi.org/10.1016/j.colsurfa.2015.02.015>
- Nobuyuki Umetani, Danny M. Kaufman, Takeo Igarashi, and Eitan Grinspun. 2011. Sensitive couture for interactive garment modeling and editing. In *ACM SIGGRAPH 2011 Papers* (Vancouver, British Columbia, Canada) (SIGGRAPH ’11). Association for Computing Machinery, New York, NY, USA, Article 90, 12 pages. <https://doi.org/10.1145/1964921.1964985>
- Jan van Ijken. 2018. Becoming. <https://www.janvanijken.com/films/becoming/>
- Bue Krogh Vedel-Larsen. 2010. *Quasi-static Simulation of Foam in the Vertex Model*. Master’s thesis. University of Copenhagen, Denmark Department of Computer Science.
- Huamin Wang. 2018. Rule-free sewing pattern adjustment with precision and efficiency. *ACM Trans. Graph.* 37, 4, Article 53 (jul 2018), 13 pages. <https://doi.org/10.1145/3197517.3201320>
- Xiaoning Wang, Xiang Ying, Yong-Jin Liu, Shi-Qing Xin, Wenping Wang, Xianfeng Gu, Wolfgang Mueller-Wittig, and Ying He. 2015. Intrinsic computation of centroidal Voronoi tessellation (CVT) on meshes. *Computer-Aided Design* 58 (2015), 51–61.
- Martin Wicke, Daniel Ritchie, Bryan M. Klingner, Sebastian Burke, Jonathan R. Shewchuk, and James F. O’Brien. 2010. Dynamic local remeshing for elastoplastic simulation. *ACM Trans. Graph.* 29, 4, Article 49 (jul 2010), 11 pages. <https://doi.org/10.1145/1778765.1778786>
- Francis Williams, Jerome Parent-Levesque, Derek Nowrouzezahrai, Daniele Panozzo, Kwang Moo Yi, and Andrea Tagliasacchi. 2020. Voronoinet: General functional approximators with local support. In *Proceedings of the IEEE/CVF Conference on Computer Vision and Pattern Recognition Workshops*. 264–265.
- Chris Wojtan, Nils Thürey, Markus Gross, and Greg Turk. 2009. Deforming meshes that split and merge. In *ACM SIGGRAPH 2009 papers*. 1–10.
- Dong-Ming Yan, Bruno Levy, Yang Liu, Feng Sun, and Wenping Wang. 2009. Isotropic Remeshing with Fast and Exact Computation of Restricted Voronoi Diagram. *Comput. Graph. Forum* 28 (07 2009), 1445–1454. <https://doi.org/10.1111/j.1467-8659.2009.01521.x>
- Dong-Ming Yan, Wenping Wang, Bruno Levy, and Yang Liu. 2011. Efficient Computation of Clipped Voronoi Diagram for Mesh Generation. *Computer-Aided Design* 45 (09 2011). <https://doi.org/10.1016/j.cad.2011.09.004>
- Guowei Yan, Wei Li, Ruigang Yang, and Huamin Wang. 2018. Inexact descent methods for elastic parameter optimization. *ACM Transactions on Graphics (TOG)* 37, 6 (2018), 1–14.
- Mariette Yvinec. 2023. 2D Triangulations. In *CGAL User and Reference Manual*. CGAL Editorial Board. <https://doc.cgal.org/5.5.2/Manual/packages.html#PkgTriangulation2>
- Jiayi Eris Zhang, Jérémie Dumas, Yun (Raymond) Fei, Alec Jacobson, Doug L. James, and Danny M. Kaufman. 2022. Progressive Simulation for Cloth Quasistatics. *ACM Trans. Graph.* 41, 6, Article 218 (nov 2022), 16 pages. <https://doi.org/10.1145/3550454.3555510>
- Xiaoting Zhang, Guoxin Fang, Chengkai Dai, Jouke Verlinden, Jun Wu, Emily Whiting, and Charlie C.L. Wang. 2017. Thermal-Comfort Design of Personalized Casts. In *Proceedings of the 30th Annual ACM Symposium on User Interface Software and Technology* (Québec City, QC, Canada) (UIST ’17). Association for Computing Machinery, New York, NY, USA, 243–254. <https://doi.org/10.1145/3126594.3126600>

A VOLUME INTEGRATION IN TETRAHEDRA

Here we provide a typical approach for volume integration over a tetrahedron, as used for analytically evaluating certain cell energy functions in this work. We consider a tetrahedron with vertices (x_i, y_i, z_i) , $i = 0, 1, 2$ and the origin. The tetrahedron can be parameterized with coordinates $(u, v, w) \in [0, 1]$ such that

$$\begin{aligned} x &= u(vx_0 + (1-v)(wx_1 + (1-w)x_2)), \\ y &= u(vy_0 + (1-v)(wy_1 + (1-w)y_2)), \\ z &= u(vz_0 + (1-v)(wz_1 + (1-w)z_2)). \end{aligned} \quad (25)$$

The Jacobian matrix of this transformation is

$$J = \begin{bmatrix} \frac{\partial x}{\partial u} & \frac{\partial x}{\partial v} & \frac{\partial x}{\partial w} \\ \frac{\partial y}{\partial u} & \frac{\partial y}{\partial v} & \frac{\partial y}{\partial w} \\ \frac{\partial z}{\partial u} & \frac{\partial z}{\partial v} & \frac{\partial z}{\partial w} \end{bmatrix} \quad (26)$$

where the partial derivatives are

$$\begin{aligned} \frac{\partial x}{\partial u} &= vx_0 + (1-v)(wx_1 + (1-w)x_2), \\ \frac{\partial x}{\partial v} &= u(x_0 - wx_1 - (1-w)x_2), \\ \frac{\partial x}{\partial w} &= u(1-v)(x_1 - x_2). \end{aligned} \quad (27)$$

A volume integral can be transformed as follows, where f^* is obtained by substituting equations 25 for (x, y, z) in f :

$$\iiint f(x, y, z) dV = \iiint_0^1 \det(J) f^*(u, v, w) dudvdw \quad (28)$$

B HESSIAN FOR BOUNDARY COUPLING

Taking the derivative of (9), we obtain the second order terms

$$\begin{aligned} \frac{d^2 E}{dc dp} &= \left(\frac{\partial x}{\partial c} \right)^T \frac{\partial^2 F}{\partial x^2} \frac{\partial x}{\partial v} \frac{dv}{dp} + \left(\frac{\partial x}{\partial c} \right)^T \frac{\partial^2 F}{\partial x \partial p} \\ &+ \frac{\partial^2 F}{\partial c \partial x} \frac{\partial x}{\partial v} \frac{dv}{dp} + \left(\sum_i \frac{\partial F}{\partial x_i} \frac{\partial^2 x_i}{\partial c \partial v} \right) \frac{dv}{dp} + \frac{\partial^2 F}{\partial c \partial p}, \\ \frac{d^2 E}{dp^2} &= \left(\frac{\partial x}{\partial v} \frac{dv}{dp} \right)^T \frac{\partial^2 F}{\partial x^2} \frac{\partial x}{\partial v} \frac{dv}{dp} + \left(\frac{\partial x}{\partial v} \frac{dv}{dp} \right)^T \frac{\partial^2 F}{\partial x \partial p} \\ &+ \frac{\partial^2 F}{\partial p \partial x} \frac{\partial x}{\partial v} \frac{dv}{dp} + \left(\frac{dv}{dp} \right)^T \left(\sum_i \frac{\partial F}{\partial x_i} \frac{\partial^2 x_i}{\partial v^2} \right) \frac{dv}{dp} \\ &+ \left(\sum_i \left(\frac{\partial F}{\partial x} \frac{\partial x}{\partial v_i} \right) \frac{d^2 v_i}{dp^2} \right) + \frac{d^2 F_B}{dp^2}, \end{aligned} \quad (29)$$

which must be added to the Hessian (7) of the fixed-boundary energy.

C DYNAMIC SIMULATION CONVERGENCE ANALYSIS

Convergence of simulations under refinement of the time step is important for assessing the accuracy of numerical solutions. To evaluate the convergence of dynamic simulations using our method, we perform a simple 2D simulation with four cells and one topological transition, illustrated in Fig. 9. The simulation is repeated for the

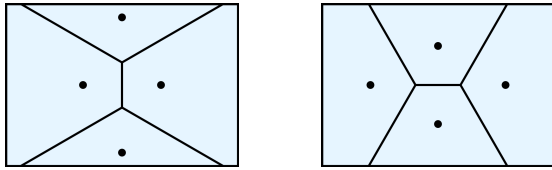


Fig. 9. Approximate initial (left) and final (right) states of a dynamic simulation used to assess the convergence of the implicit Voronoi model.

same total time using a range of time steps. Error measurements in Fig. 10 show that given a sufficiently smooth energy function and using second-order finite difference approximations (BDF2),

the dynamic simulation method presented in section 3.7 converges quadratically. Linear convergence is achieved for C^0 -continuous energy functions (such as perimeter and surface area) or using only a first-order accurate acceleration.

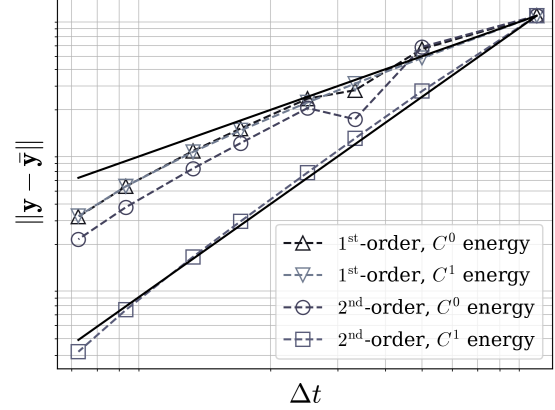


Fig. 10. Final state error vs. time step for a simple 2D case including a topological transition. Final state from highest resolution simulation is taken as ground truth \bar{y} . Solid lines represent exact linear and quadratic convergence, with steeper slope indicating higher-order convergence.

D EXPERIMENT DETAILS

In this section we provide additional details and parameters required to reproduce the examples in Sec. 4.

Intercellular Navigation with Rigid Body. The domain is rectangular with width 4m and height 2m, containing $n = 2000$ cells along with the rigid body. Other parameters are $\bar{A} = 0.004 \text{ m}^2$, $a_0 = 0.05 \text{ N/m}^3$, $a_1 = 100.0 \text{ N/m}^3$, $a_2 = 1.0 \text{ N/m}$, $F_x = 0.035 \text{ N}$, $h = 0.01 \text{ s}$, $m_c = 0.0003 \text{ kg}$, $m_p = 0.0003 \text{ kg}$, $\eta_c = 0.0003 \text{ N s/m}$, $\eta_p = 0.003 \text{ N s/m}$. Here and in the following examples, m and η are diagonal entries of the mass matrix \mathbf{M} and viscosity matrix $\boldsymbol{\eta}$ corresponding to the site (c) and boundary (p) degrees of freedom.

Foam Coarsening. The domain is a $2\text{m} \times 2\text{m} \times 20\text{cm}$ box starting with $n = 2000$ cells. Other parameters are $\bar{V}_{\text{initial}} = 0.0004 \text{ m}^3$, $a_0 = 0.002 \text{ N m}$, $a_1 = 0.01 \text{ N/m}$, $a_2 = 0.1 \text{ N/m}$, $\eta_c = 0.0001 \text{ N s/m}$, $\eta_{\bar{v}} = 1.0 \text{ N s/m}^3$. The time step $h = \frac{1.0}{n} \text{ s}$ is adapted each frame to the number of remaining cells n , increasing as the rate of cell collapse slows.

Embryonic Cleavage. The initial domain is an *icosphere* with 4 subdivisions, approximating a sphere with radius 1.34m. Other parameters are $\bar{V}_{\text{initial}} = 10.25 \text{ m}^3$, $a_0 = 50.0 \text{ N m}$, $a_1 = 5.0 \text{ N}$, $a_2 = 1.0 \text{ N m}$, $h = 0.01 \text{ s}$, $\eta_c = 5.0 \text{ N s/m}$, $\eta_p = 0.5 \text{ N s/m}$, $\beta = 0.1$.

Tissue Proliferation in Cylinder. The initial domain is a cylinder of radius 1m whose upper deformable face comprises 2432 triangles. Other parameters are $\bar{V}_{\text{initial}} = 0.113 \text{ m}^3$, $a_0 = 10.0 \text{ N m}$, $a_1 = 10.0 \text{ N}$, $a_2 = 1.0 \text{ N m}$, $h = 0.01 \text{ s}$, $\eta_c = 0.5 \text{ N s/m}$, $\eta_p = 0.003 \text{ N s/m}$, $\alpha = 30 \text{ m}^{-3} \text{ s}^{-1}$, $\beta = 0.1$, $\gamma = 0.75$, $\tau = 0.11 \text{ s}$.